Materials and Design 196 (2020) 109146

Contents lists available at ScienceDirect

Materials and Design

journal homepage: www.elsevier.com/locate/matdes

# Nanoparticle-induced growth behavior of primary α-Mg in AZ91 alloys

Haonan Li [a,b], Kui Wang [a,b,*], Gaopeng Xu [a,b], Haiyan Jiang [a,b,*], Qudong Wang [a,b], Wenjiang Ding [a,b]

[a] National Engineering Research Center of Light Alloy, Net Forming, Shanghai Jiao Tong University, 200240 Shanghai, PR China
[b] State Key Laboratory of Metal Matrix Composites, Shanghai Jiao Tong University, 200240, Shanghai, PR China

## HIGHLIGHTS

- The addition of TiCN NPs can lead to a significant refinement of primary α-Mg and eutectic β-$Mg_{17}Al_{12}$ in AZ91 alloys.
- The growth control induced by multi-layer of NPs covering the surface of α-Mg could be the main refining mechanism.
- NPs can reduce grain growth velocity, promote nucleation events andgrain impingement, inducing significant grain refinement.

## GRAPHICAL ABSTRACT

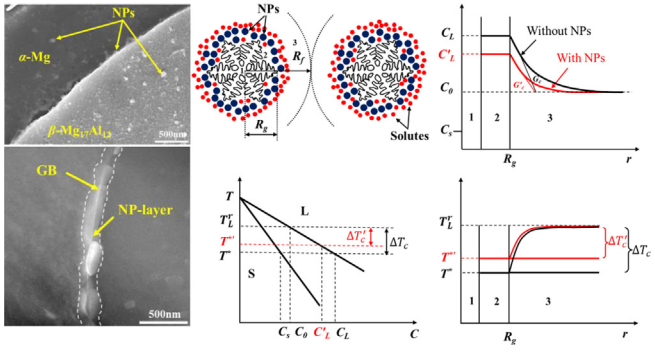


## ARTICLE INFO

*Article history:*
Received 16 July 2020
Received in revised form 23 August 2020
Accepted 9 September 2020
Available online 10 September 2020

*Keywords:*
Grain refinement
NP-induced growth control
Solute concentration gradient
Grain impingement

## ABSTRACT

Significant grain refinement of AZ91 alloys was achieved by ceramic nanoparticle(NP)-induced growth control. Advanced characterization techniques including 3D tomography and in-situ observation were carried out to examine the microstructure evolution. The results show that the NPs are distributed in matrix in three ways, i.e. along the grain boundaries, inside the α-Mg grains and within the interior of β phases. The intergranular NPs that are distributed along the grain boundaries can form a multilayer of NPs covering the surface of α-Mg, greatly restricting the grain growth. A numerical model is proposed to predict the grain size, in which the solute concentration gradient at dendrite tip and the impingement of grains are recognized as two pivotal factors in modelling. It is demonstrated from the model prediction that a reduced growing rate of α-Mg can be obtained upon NP addition due to the lowered solute concentration gradient at dendrite tip, which could increase the nucleation events, accelerate the grain impingement and thus induce significant grain refinement. Given the chemically and thermally stability of ceramic NPs, which can avoid the intrinsic drawbacks of conventional inoculation, e.g. element poisoning, NP-induced growth control (NIGC) may provide a new avenue for grain refinement in magnesium alloys.



## 1. Introduction

A combination of light weight, good plasticity, high specific strength and stiffness makes magnesium alloys one of the most promising and widely-applied metallic structural materials in the last few decades [1–3]. With increased development and usage of magnesium alloys, magnesium alloys with enhanced performance are increasingly required. Nowadays, it is well-accepted that grain refinement is one of the most effective approaches to improving the mechanical properties of magnesium alloys [4]. Although it can be achieved by addition of various nucleating particles including SiC, $Al_4C_3$, AlN, $Al_2Y$ etc. [5–9], there still remain intractable issues such as element poisoning and poor refining efficiency for specific magnesium alloys like AZ series. For example, Zr is well-established for its high growth restriction factor (Q-value) of 38.29 [10], which implies that the constitutional supercooling (CS) zone can be built up at a high rate, leading to fine grains. But it only

* Corresponding authors at: National Engineering Research Center of Light Alloy, Net Forming, Shanghai Jiao Tong University, 200240 Shanghai, PR China.
*E-mail addresses:* fateratory@sjtu.edu.cn (K. Wang), jianghy@sjtu.edu.cn (H. Jiang).

https://doi.org/10.1016/j.matdes.2020.109146

works with Al/Mn/Si-free alloys due to the formation of intermetallics with Al, Mn and Si that have a poor crystallographic matching with the magnesium matrix [4]. Moreover, the grain-refining efficiency by nucleating particles is so low that only less than 1% of the particles can participate in a nucleation event [11]. What is worse, refining efficiency decreases dramatically with the increase of particle addition level. Therefore, it is of great necessity to adopt a new strategy to tackle these problems associated with magnesium alloys.

Most recently, nanoparticles (NPs) reinforced light metal alloys have attracted increasingly more attention [12,13]. Apart from the utilization of NPs as reinforcements, many efforts have been undertaken to control the microstructure by NPs and significant microstructure improvement has been achieved in this way [14–16]. The charged NPs were initially discovered as the functional universal surfactants to induce a slow crystal growth by the formation of NP layer on the crystal surface [17]. Afterwards, ceramic nanoparticles were employed to refine the microstructure of Sn—Al and Al—Si alloys and found to restrict the growth of primary α-Al phases [18,19]. It is possibly because solute transport during solidification could be retarded through the NP assembly onto the advancing interface. It was reported that when 0.7 wt% NPs were incorporated in Mg-25Zn-7Al (wt%) alloys, the effective diffusivity of zinc could be decreased by about one-third as compared to that for NP-free alloys, which resulted in a reduction of 33% in grain size [20]. Additionally, given that ceramic nanoparticles are much more chemically and thermally stable than refining elements like Zr, the element poisoning and detrimental reaction products would be radically avoided. Therefore, NP-induced growth control (NIGC) may pave a novel avenue for grain refinement of magnesium alloys.

To clarify the mechanisms underlying NP-induced crystal growth, an irreversible adsorption model was firstly proposed by Kowalczyk et al. [17]. Then, it was modified by Chen et al. [21] who employed it to describe the phase growth kinetics influenced by NPs in immiscible Al—Bi alloys. Subsequently, Wang et al. [19] extended it to the condition of equiaxed dendritic growth at different cooling rates in hypoeutectic Al—Si alloys. As far as these models are concerned, the characteristic time for NP assembly onto the phase surface $t_{np}$ and the diffusion-hindrance efficiency $f$ are acknowledged as two critical factors in the modelling. For the former, the time factor is inversely proportional to NP addition. The infinitesimal $t_{np}$ of about several milliseconds manifests a high efficiency for NP coverage. For the latter, the diffusion-hindrance efficiency is used as an indicator of NP effect on the phase growth, which is proportional to NP addition. As pointed out by Wang et al. [19], $f$ is in essence a synthetical reflection of the growth restriction caused not only by NP assembly, but also by the impingement of the growing phases. However, the contribution of impingement to growth restriction is not considered in previous models. Although in the early stages of solidification, each grain is isolated from each other and can grow freely, impingement of growing grains stifle further growth as solidification proceeds [22,23]. With the developing dendritic grains impinging on the neighboring ones, a coherent dendrite network can be established. The interaction between growing grains is thus another important mechanism by which grain growth is restricted. For an in-depth understanding of the grain growth mechanisms in NP-containing alloys, it is of great significance to investigate the effects of impingement and NPs on grain growth.

In the present work, advanced characterization techniques including 3D tomography and in-situ observation were carried out to examine the microstructure evolution in NP-containing AZ91 alloys. Unlike the works by D. H. St John et al. [24], where grain refinement can be attained by applying ultrasonic treatment over a solidified temperature range during or after nucleation of primary grains, the ultrasonication treatment was adopted to disperse NPs in the melt at a given temperature above the liquidus, which is invalid before nucleation. The effect of NP addition on the growth behavior of primary α-Mg was discussed systematically from the perspective of heterogeneous nucleation and growth restriction. A theoretical model is first established to unveil the combined roles of NPs and impingement on the grain growth.

## 2. Materials and experimental methods

### 2.1. Sample preparation

AZ91 alloys and $TiC_{0.3}N_{0.7}$ ceramic nanoparticles with a diameter of 50 nm were used in this study. The matrix alloys were prepared by placing commercial high pure magnesium (99.9% purity), aluminum (99.5%) and Zinc (99.9%) into a graphite crucible and melting at 720 °C in an electric resistance furnace. The mixture of $CO_2/SF_6$ with ratio of 1:2 was used as a protective gas. For the removal of gases and inclusions, the melt was heated at 740 °C and then degassed using the mixture of $MgCl_2$, KCl, $BaCl_2$ and $CaF_2$ (1.0 wt%). After skimming off the oxide skin, $TiC_{0.3}N_{0.7}$ nanoparticles wrapped in aluminum foils (the mass of the foil is also considered in the final material composition) were submerged beneath the surface of the melt at 720 °C for 10 min. The ultrasonication was applied to disperse nanoparticles. The tip of ultrasonic probe was dipped into the melt about 10 mm in depth and the ultrasonic treatment was carried out at the temperature of 700 °C for 20 min. After the completion of ultrasonication, the probe was removed out of the melt. The melt was heated to 720 °C before pouring into a preheated cylindrical permanent mold (300 °C). It should be noted that there is no ultrasonication during the casting process. In this work, $TiC_{0.3}N_{0.7}$ nanoparticles were adopted as growth inhibitors because of their high density, high chemical and thermal stability, strong oxidation resistance and better compatibility with the metal matrix [21,25]. Various volume fractions of TiCN nanoparticles (0.5, 1.0, 1.5, 2.0 and 2.5 vol%) were incorporated into AZ91 alloys. For the purpose of comparison, a matrix alloy without NP addition was also prepared under the same condition.

### 2.2. Measurement of cooling curves

The effects of different cooling rates on the growth behavior of primary α-Mg were investigated after addition of nanoparticles. The variations of the temperature with time during solidification were measured by K-type thermocouples placed inside the castings and then recorded by data acquisition system. For the permanent mold mentioned in Section 2.1, the cooling rate was calculated to be about 5 K/s. Besides, to obtain different cooling rates, the melt was cast into a graphite crucible and then cooled either in air or in furnace. The measured cooling rates were approximately 1 K/s and 0.1 K/s, respectively. The characteristic temperatures of solidification can be determined from the time integration ($dT/dt$) and three characteristic temperatures were given in this work [26–28], i.e. the nucleation temperature ($T_N$), defined as the first remarkable change in the first derivative of cooling curve or the minimum point of the valley just before the perceptible peak in the second derivative curve; the minimum temperature before recalescence ($T_m$); and the nucleation undercooling ($\Delta T_N$), defined as $\Delta T_N = T_N - T_m$.

### 2.3. Material characterization

The metallographic specimens were sectioned from the center of the castings, mechanically polished, and then etched in the mixture solution of 1 ml acetic acid, 150 ml ethanol and 50 ml highly purified water. The etched samples were imaged using a polarized light optical microscope. The grain sizes were measured using the linear intercept method. Polyfunctional X-Ray Diffractometer (XRD) with voltage of 40 kV and current of 40 mA was used for phase identification. The step size is 0.02° and the scan angles is a range of 10–90°. The microstructures of samples were observed using

TESCAN-MAIA3 field emission scanning electron microscopy (FESEM) with voltage of 5 kV. The TEM analysis was carried out to examine the distribution of nanoparticles and their crystallographic orientations with primary α-Mg using transmission electron microscopy

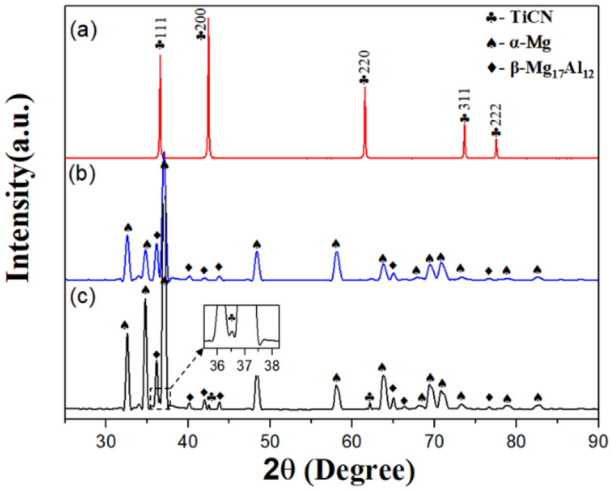


**Fig. 1.** XRD patterns of (a) NPs; (b) Matrix alloy; (c) AZ91 alloy with 2 vol% NP addition.

(TEM; Talos F200X G2) with voltage of 200 kV on the TEM foils prepared using Precision Ion Polishing system (PIPS, Gatan 695).

The 3D tomography analysis was performed using Zeiss Xradia 520 Versa device. The specimens for 3D tomography observation were cylinders with 0.7 mm in diameter and 5 mm in height. The voltage and electric power were 60 kV and 5 W, respectively. The images of projection were captured at an interval of 0.11° over a total range of 360°. The exposure time was 2500 ms. The voxel resolution used in this measurement is 0.7 μm, which is applicable to the observation of β phases with the size more than 1 μm. The data files containing three-dimensional information were processed using Dragonfly software, including image segmentation and 3D mesh reconstruction of different phases.

In-situ observation of the growth of primary α-Mg under different cooling rates during solidification were accomplished using Ultrahigh Temperature Confocal Scanning Laser Microscope. The experimental samples have a size of φ 7.5 mm × 3.0 mm, whose two base surfaces were polished. Each sample was deposited in a ceramic crucible and then heated up ~50 °C above the liquidus temperature for 10 min until it was completely melted. The heating chamber was filled with argon to prevent oxidation. The melts were cooled to room temperature at three given cooling rates, i.e. 0.1 K/s, 1.0 K/s and 5.0 K/s.

## 3. Results

### 3.1. Grain refinement with nanoparticles

Fig. 1 shows the XRD analysis of $TiC_{0.3}N_{0.7}$ nanopowder and as-cast AZ91 alloys with and without NP addition. As shown in Fig. 1(a), five strong diffraction peaks of NPs can be identified at the 2-Theta ranging from 25° to 90°, and the corresponding indices of lattice planes vary from {111} to {222}, among which the diffraction peak intensity of {200} is strongest, followed by {111} and {220}. Fig. 1(b) presents the phase composition of the matrix alloy and it is composed of primary α-Mg and eutectic β-$Mg_{17}Al_{12}$. After the addition of NPs, three strong peaks of $TiC_{0.3}N_{0.7}$ phases concordant with Fig. 1(a) can be observed in Fig. 1(c), which confirms the existence of $TiC_{0.3}N_{0.7}$ nanoparticles in the sample.

The anodized micrographs of the samples with different NP additions prepared at the same cooling rate of 5 K/s are showed in Fig. 2. Fig. 2(a) exhibits the grain microstructure of matrix alloy characterized by coarse equiaxed dendritic grains with the average size of 108 μm. After the addition of 0.5 vol% NPs, the average grain size is decreased to 87 μm. With the further addition of NPs, the variation of grain sizes continues a declining trend until reaching the minimum of 36 μm at the addition level of 2 vol%, which is approximately 66.3% smaller than that of matrix alloy. It should be noted that very high NP addition levels, i.e. more than 2.0 vol% can not lead to further grain refinement as shown in Fig. 3(a). It may be ascribed to the agglomeration of NPs at high addition levels. It can be speculated that NP aggregates or

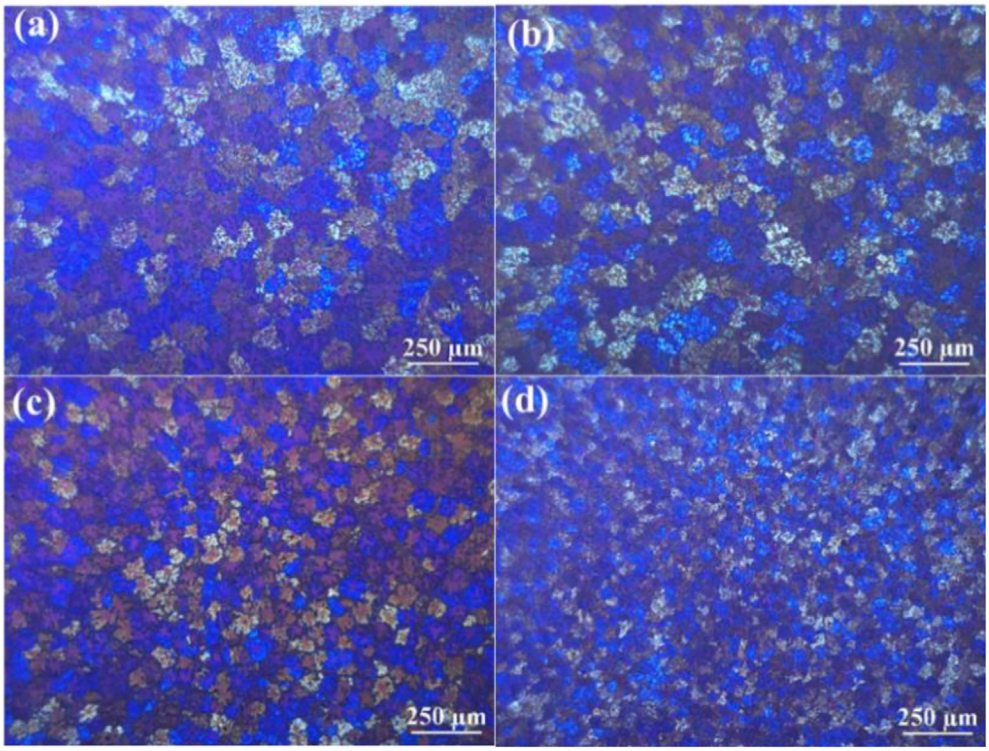


**Fig. 2.** The anodized micrographs of as-cast AZ91 alloys with various NP addition levels. (a) Matrix alloy; (b) 0.5 vol%; (c)1.0 vol%; (d) 2.0 vol%.

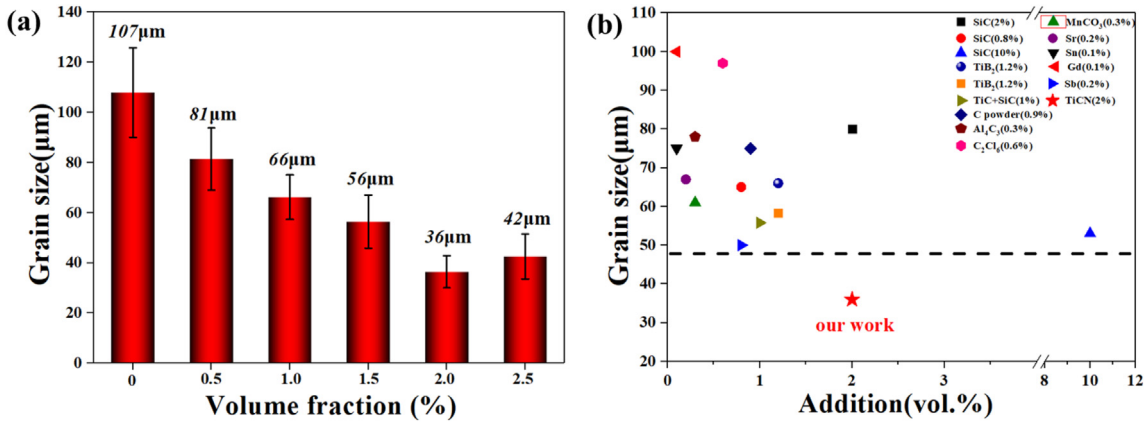


**Fig. 3.** (a) The average grain size of AZ91 alloys vs NP addition levels; (b) The comparison of grain sizes between the present work and the experimental results reported in literature.

clusters are likely to compromise the refining effect. For comparison with the refining effects of various refiners in AZ91 alloys, including particles and elements, the relevant experimental information in the literature is listed in Table 1 and the comparison of results is shown in Fig. 3 (b). It can be seen that the NP-induced growth control can result in the most remarkable refining effect in AZ91 alloys nowadays.

### 3.2. Refinement of β-$M_{17}Al_{12}$ phases

Fig. 4 shows the eutectic microstructure of matrix alloy and AZ91 alloy with 2 vol% NP addition. The bright phases are eutectic β-$M_{17}Al_{12}$ while the dark ones are primary α-Mg. From Fig. 4(a) and (b), it can be seen that the coarse β phases in the matrix alloy are characterized by the network structure and precipitate along the grain boundaries of primary α-Mg. Some of them are in the form of lamellar structure. The addition of 2.0 vol% NPs leads to the morphological transition of β phases from coarse continuous to fine discontinuous network structure as shown in Fig. 4(c) and (d). Furthermore, it is clear from Fig. 4(d) that a majority of nanoparticles are found to be distributed along the grain boundaries of primary α-Mg.

To evaluate the extent to which NPs can affect the morphology, distribution and fraction of β phases, 3D tomography analysis has been performed, which is expected to provide more comprehensive information on their network structure than the characterization by 2D images. The spatial structures of β phases in the matrix alloy and the sample containing 2.0 vol% NPs are illustrated in Fig. 5. The primary α-Mg phases are colored in blue while the β-$M_{17}Al_{12}$ phases are visualized in green. Fig. 5(a) displays the cuboid reconstruction map of the matrix alloy. It is evident that β phases are distributed intricately along the grain boundaries of α-Mg. Fig. 5(b–g) represent the morphology and distribution of primary and eutectic phases extracted from Fig. 5(a). The 2D images, as shown in Fig. 5(b–d), are the basis of reconstruction, extraction and visualization of the partial three-dimensional microstructure, including separate 3D morphologies of primary α-Mg phases and β-$M_{17}Al_{12}$ phases. The typical α-Mg equiaxed dendrites with coarse dendrite arms can be observed in Fig. 5(f). By contrast, there is a marked reduction in the length of dendrite arms of α-Mg in NP-containing sample, some of which even transform from dendritic to spherical grains in Fig. 5 (m). After removing the primary phases, the coarse and continuous 3D network structure of β phases can be clearly demonstrated in Fig. 5 (g). Compared with the matrix alloy, the β phases in NP-containing sample exhibit more homogeneous spatial distribution and refined morphology as depicted in Fig. 5(n). Fig. 6(a) and (b) present the 3D morphologies of β phases extracted from Fig. 5(a) and (h), respectively. By comparison, it is can be seen that the NP addition can lead to a uniform and dispersive distribution of β phases in the matrix. Also clear from Fig. 6(c) is that the volume fraction and specific surface area of β phases are both increased after the NP addition. The experimental results show that the NP addition can lead to the reduction in α-Mg and β-$Mg_{17}Al_{12}$ sizes. The refinement of α-Mg may be mainly attributed to NP addition while the refinement of β-$Mg_{17}Al_{12}$ may be a by-product of finer primary α-Mg, which is further discussed in Section 4.1.

### 3.3. Characterization of nanoparticles

Fig. 7 shows the SEM micrographs of AZ91 alloys with 2.0 vol% NP addition. As shown in Fig. 7(a) and (b), a large proportion of NPs are located at the interfaces between primary α-Mg and β-$Mg_{17}Al_{12}$. These

**Table 1**
Various grain refinement methods of AZ91 alloys reported in literature [29–41].

| Matrix | Refiner | Addition level | Method | State | Grain size (μm) | Ref |
|---|---|---|---|---|---|---|
| AZ91 | AlN | – | Gravity casting | As-cast | 50 | [7] |
| | TiC and SiC | 1 vol% | Ultrasonication+Gravity casting | As-cast | 55.79 | [29] |
| | MnCO3 | 0.6 wt% | Gravity casting | As-cast | 61 | [30] |
| | Sr | 0.2 wt% | Gravity casting | As-cast | 67 | [31] |
| | SiC | 2 vol% | Ultrasonication+Gravity casting | As-cast | 80 | [32] |
| | SiC | 1.5 wt% | Ultrasonication+Gravity casting | Solid solution | 65 | [33] |
| | SiC | 10 vol% | Gravity casting | As-cast | 53 | [34] |
| | Al-$TiB_2$ master alloy | 2.5 wt% | Semi-solid mechanical stirring+Gravity casting | As-cast | 66 | [35] |
| | Al-$TiB_2$ master alloy | 2.5 wt% | Semi-solid mechanical stirring+Gravity casting | Solid solution | 58.4 | [35] |
| | C powder | 1 wt% | Gravity casting | Solid solution | 75 | [36] |
| | Sn | 0.5 wt% | Gravity casting | – | 75 | [37] |
| | Gd | 0.5 wt% | Gravity casting | As-cast | 100 | [38] |
| | Sb | 0.5 wt% | Gravity casting | As-cast | 93 | [39] |
| | In-situ TiC-$TiB_2$ | – | Semi-solid mechanical stirring+Gravity casting | Solid solution | 72 | [40] |
| | $Al_4C_3$ | 0.5 wt% | Gravity casting | As-cast | 78 | [41] |

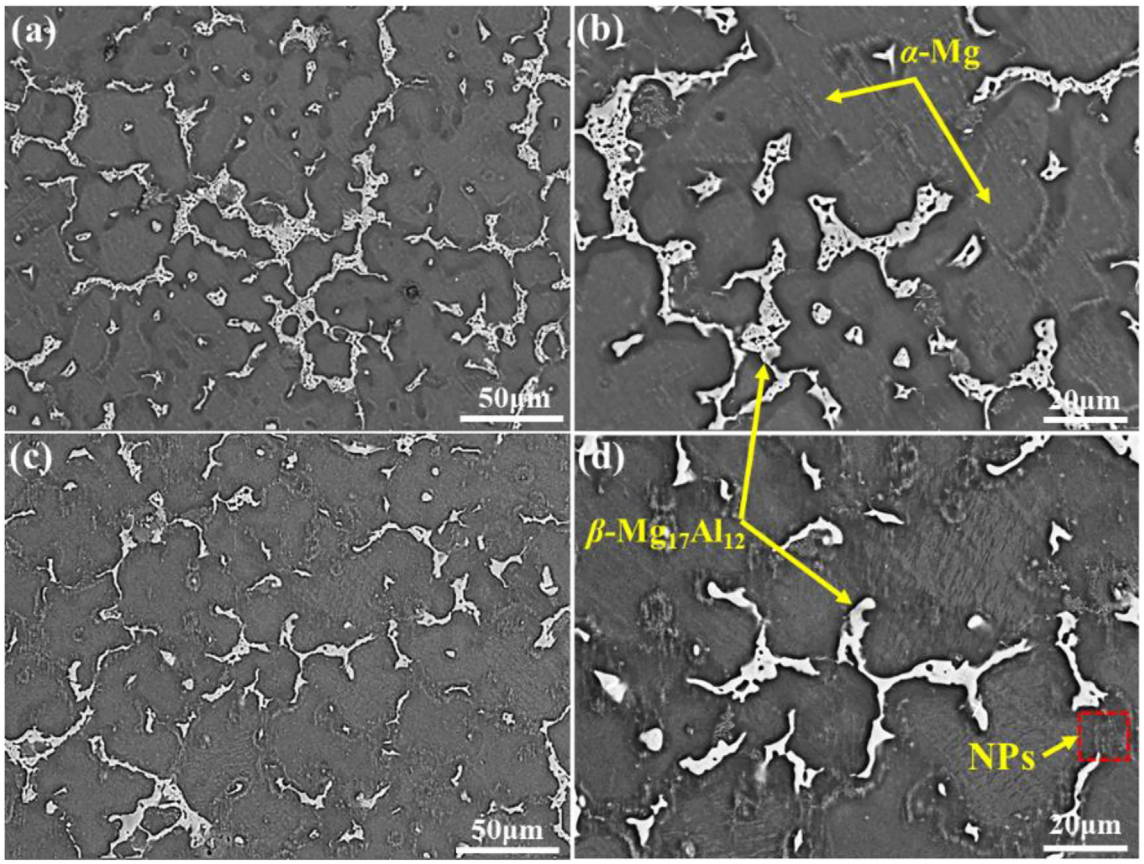


**Fig. 4.** SEM micrographs of AZ91 alloys with different NP addition levels: (b) and (d) magnified from (a) Matrix alloy and (c) 2 vol% NP addition, respectively.

nanoparticles segregate intergranularly to form a densely-packed layer covering the surface of α-Mg, which may be effective in inhibiting solute atoms from transporting onto the growing interface, restricting its growth and thus refining its grain size. Apart from the intergranular distribution, many NPs are found to be distributed within α-Mg dendrites and β phases as shown in Fig. 7(c) and (d). For the former, a small fraction of NPs may be captured by the growing α-Mg dendrites during solidification. There are several factors behind the NP capture, including melt viscosity and local solidification rate. An increase in NP addition level may increase the melt viscosity and thus the viscous force acting on NPs, facilitating the NP capture. In addition, the local positions like the mold wall may provide high solidification rate to promote the NP capture. For the latter, as the grain growth proceeds, a majority of NPs may be pushed by the advancing dendrite to the intergranular regions where the eutectic reaction would occur once the eutectic temperature could be reached. With the β phases precipitating along the grain boundaries, these NPs inevitably assemble onto their surface and are distributed inside them eventually.

The bright-field TEM images and STEM mapping in Fig. 8(a–c) further reveal that the nanoparticles with an average diameter of 50 nm are distributed in the matrix in three ways, i.e. along the grain boundaries, inside the α-Mg grains and within the interior of β phases. As shown in Fig. 8(d), nanoparticles that are embedded in the interior of α-Mg exhibit random crystallographic orientation relationships (ORs) with the α-Mg matrix. Some of them are found to be coherent with the matrix. Fig. 8(e) displays a nanoparticle located in between α-Mg and β phase, and two interfaces can be clearly observed. According to the crystallographic information provided by the fast Fourier transformation (FFT) of the nanoparticle and α-Mg in Fig. 8(g–i), there exists a coherent interface between the nanoparticle and the α-Mg matrix, and the OR is obtained as $[2\bar{1}\bar{1}0]_{\alpha\text{-Mg}}//[011]_{NP}$, $(0002)_{Mg}//(11\bar{1})_{NP}$. Conversely, an incoherent interface is formed between the nanoparticle and β phase. Fig. 8(f) exhibits another nanoparticle located at the grain boundary of α-Mg. The incoherent interface between them confirms that the intergranular nanoparticles also have random ORs with the α-Mg matrix. Furthermore, the interfaces between NP and α-Mg and between NP and β phase are smooth and taintless with no intermetallics formed, whether they are coherent or incoherent. It is noteworthy that the coherent interface may provide a strong interfacial bonding between the NP-layer and the growing phase, leading to a pronounced growth-restricting effect.

### 3.4. Effects of cooling rates on microstructure evolution

Fig. 9 shows the measured cooling curves of the matrix alloy and the sample with 2.0 vol% NP addition produced at three given cooling rates, i.e. 0.1, 1 and 5 K/s. Two plateaus can be observed on each curve, which represent the nucleation and growth of primary α-Mg dendrites and eutectic β-$M_{17}Al_{12}$ phases [42]. The time integration ($dT/dt$) of each curve is calculated and shown at the bottom of each figure. The three characteristic temperatures as mentioned in Section 2.2 are listed in Table 2. From the measured data, it can be seen that $T_N$ of α-Mg increases with the cooling rate while $T_m$ decreases with it. As a result, the nucleation undercoolings $\Delta T_N$ exhibits an increasing trend with the cooling rate as $\Delta T_N = T_N - T_m$. After incorporating NPs into AZ91 alloys, there is a slight increase in $T_{N,\alpha\text{-Mg}}$ for any given cooling rate. It can be inferred that the NP addition may have little effect on the nucleation temperature of primary α-Mg. However, a significant reduction occurs to $T_{m,\alpha\text{-Mg}}$ for NP-containing sample. It may be principally attributable to the decline in the release of latent heat during the restricted growth of α-Mg induced by NPs. The decreased $T_{m,\alpha\text{-Mg}}$ could lead to a great increase in the nucleation undercooling, and the heterogeneous

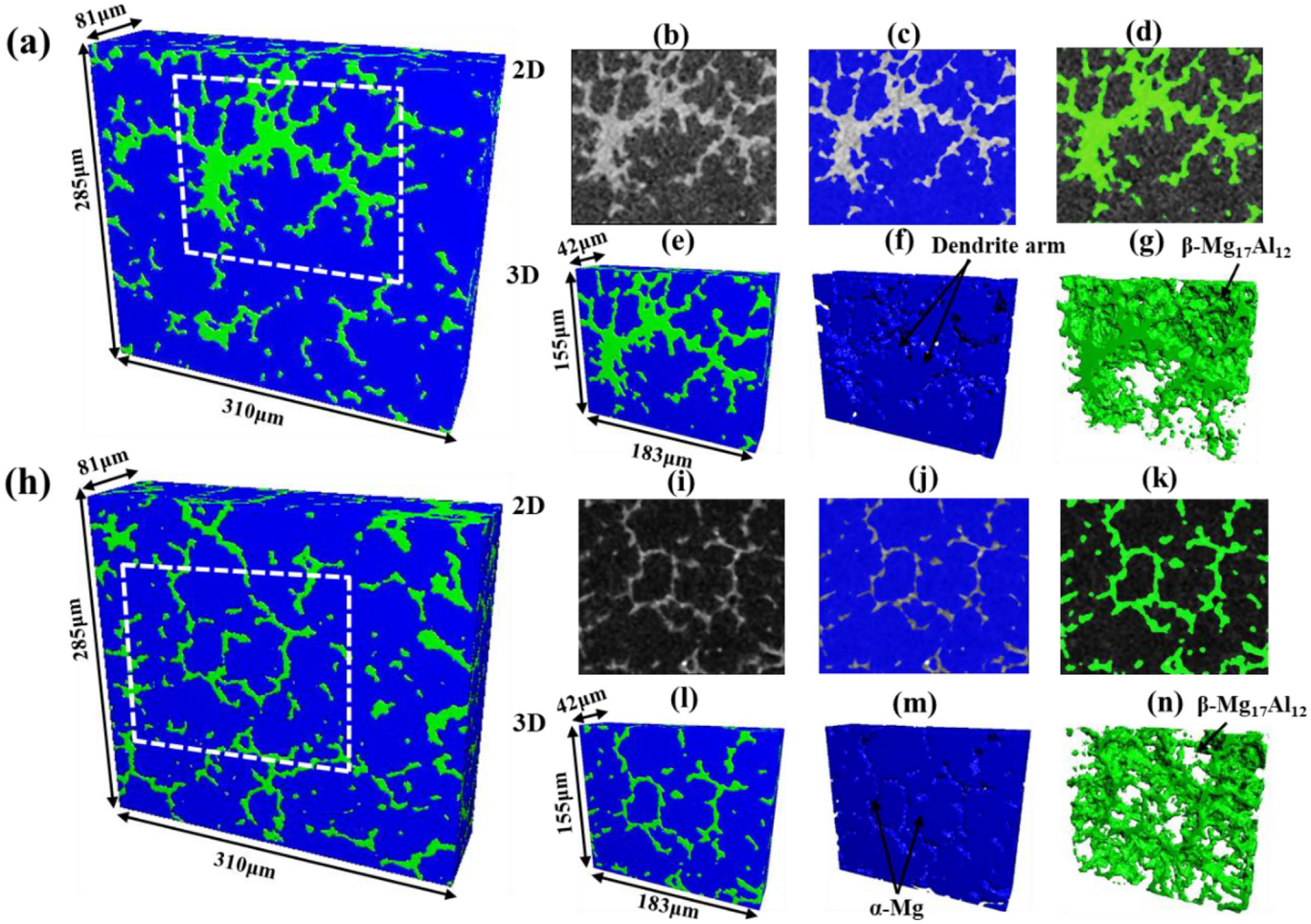


**Fig. 5.** Three-dimensional morphology of the matrix alloy and the sample with 2 vol% NP addition: (a) Matrix alloy; (h) 2 vol%; (b−d) and (i-k) 2D images extracted from (a) and (h), respectively; (e–g) and (l–n) 3D images extracted from (a) and (h), respectively.

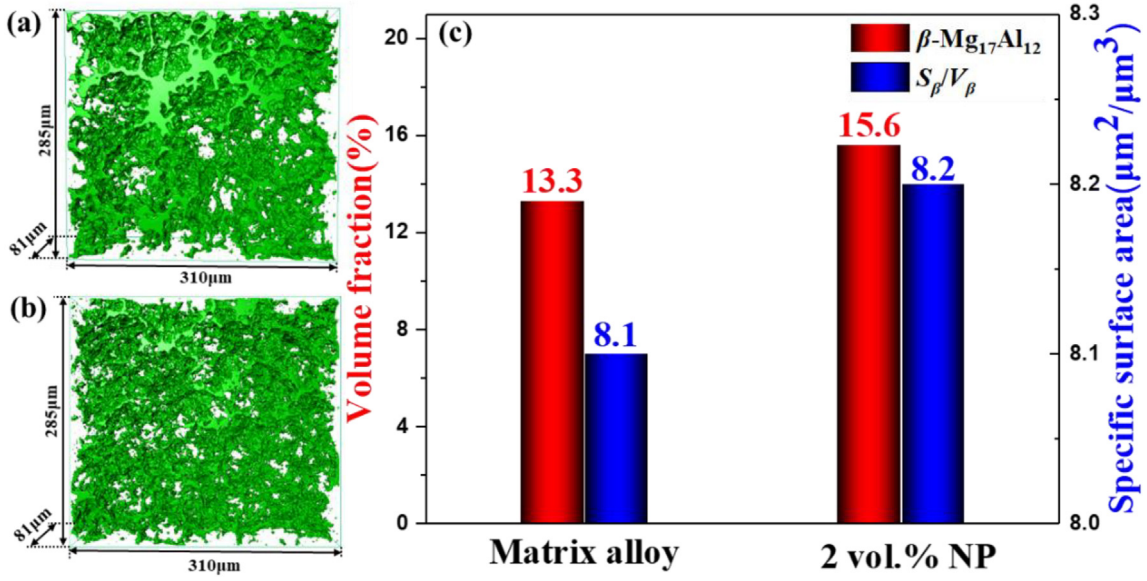


**Fig. 6.** 3D morphologies of separated β-$M_{17}Al_{12}$ phases in a cuboid with the size of 310 μm × 81 μm × 285 μm: (a) Matrix alloy; (b) Sample with 2 vol% NP addition; (c) Comparison of volume fraction and specific surface area of β-$M_{17}Al_{12}$ phases between the matrix alloy and 2 vol% NP-containing sample.

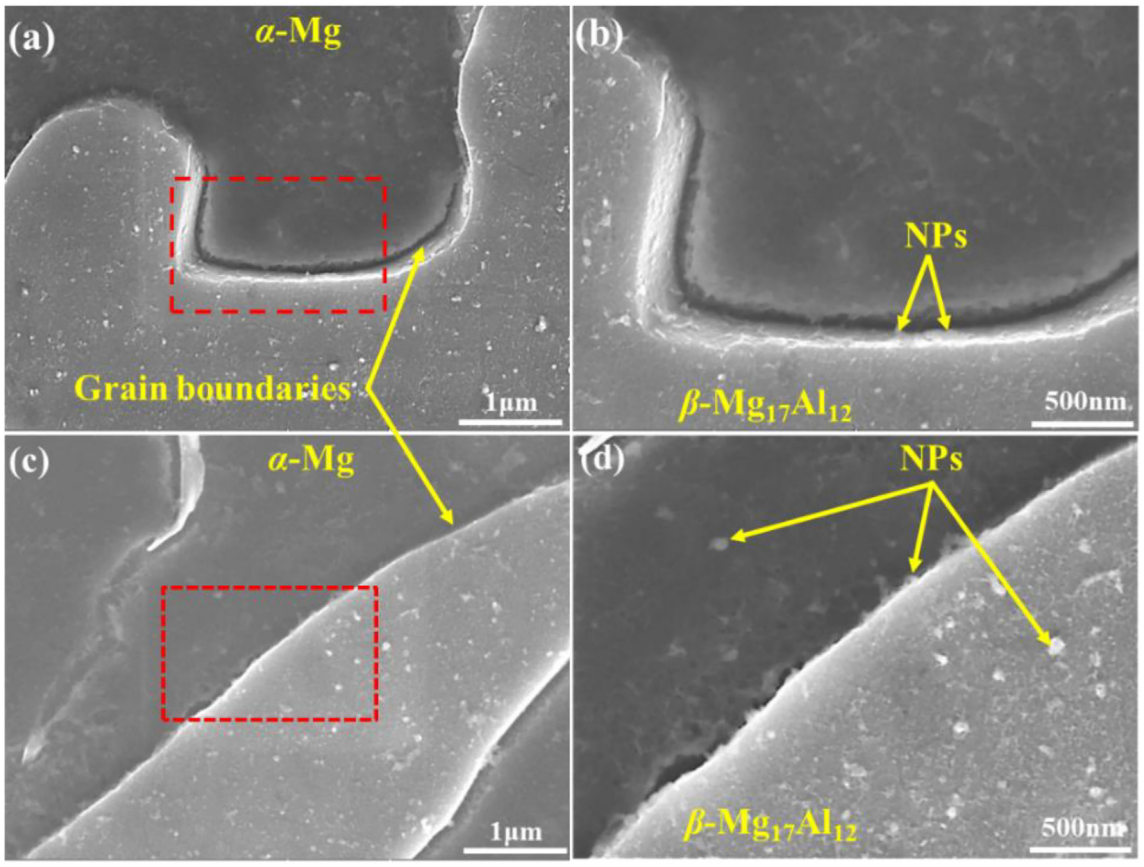


**Fig. 7.** (a) SEM micrographs of AZ91 alloys with 2 vol% NP addition: (b) and (d) magnified from (a) and (c), respectively.

nucleation of α-Mg is thus promoted. Similarly, the three characteristic temperatures of eutectics in NP-containing sample exhibit almost the same varying tendency as that of α-Mg. It is noteworthy that unlike the slight variation of $T_{N,\alpha\text{-}Mg}$, there is a remarkable increase in $T_{N,eu}$ for three given cooling rates. It may be mainly due to the growth restriction caused by the presence of nanoparticles along grain boundaries, which can hamper the growth of eutectic phases, thus leading to the enhanced nucleation of eutectics.

To unveil the combined effects of NP addition and cooling rates on the microstructural evolution of AZ91 alloys, in-situ observation of the solidification processes of the matrix alloy and 2 vol% NP-containing sample has been carried out and the results are shown in Figs. 10 and 11. The entire solidification process can be divided into three stages: the beginning of nucleation at 600 °C, the growth of primary α-Mg at 500 °C and the completion of eutectic reaction at 400 °C. As shown in Figs. 10(a, d, g) and 11(a, d, g), several α-Mg nuclei emerged in the melts at the first stage for the matrix alloy and NP-containing sample under the cooling rates of 1 K/s and 5 K/s, respectively. As solidification proceeded, an increasing number of primary α-Mg grains started to nucleate and grew during a short period. When the temperature reached 500 °C, the growth of α-Mg grains at the second stage seemed to be spherical and not dendritic for the matrix alloy solidified at the cooling rate of 0.1 K/s as shown in Fig. 10(b). However, the dendritic growth of α-Mg grains could be discernible at high cooling rates of 1 K/s and 5 K/s in Fig. 10(e) and (h), respectively. Compared with the matrix alloy, significantly refined α-Mg dendrites could be achieved at any given cooling rates through the addition of TiCN nanoparticles as presented in Fig. 11(b,e,h). Moreover, the interdendritic or intergranular regions between primary α-Mg grains, i.e. the dark regions shown in Figs. 10 (b,e,h) and 11(b,e,h) were filled with the residual metal liquid that was trapped by solid networks. Then the eutectic reaction would occur in these regions. As the temperature declined to 400 °C, the solidification process came to an end with the precipitation of β-$Mg_{17}Al_{12}$ phases along the grain boundaries. As illustrated in Fig. 10(c,f,i) and 11(c,f,i), the morphologies of α-Mg grains could be clearly observed at the end stage. Interestingly, a morphological transition of α-Mg grains from spherical at 500 °C in Fig. 10(b) to dendritic at 400 °C in Fig. 10 (c) took place. More interestingly, when the cooling rate was raised from 0.1 to 5 K/s, the α-Mg grains in the NP-containing sample transformed from refined equiaxed dendrites (Fig. 11(c)) to fine equiaxed dendrites (Fig. 11(f)) and eventually to finer spherical grains (Fig. 11 (i)). In conclusion, the in-situ observation results demonstrate that the NP-induced grain refinement can be further improved with increasing the cooling rates from 0.1 to 5 K/s.

## 4. Discussion

### *4.1. Microstructural refinement mechanisms induced by nanoparticles*

According to the microstructural observation, the presence of nanoparticles in the matrix has a significant influence on the α-Mg grain size, and the NIGC is highly likely to be the main mechanism underlying the grain refinement. Nevertheless, there is no denying the fact that the added nanoparticles might be involved in the nucleation event as the nucleating particles. In general, particles can be taken as potent nucleating particles if two basic requirements can be fulfilled simultaneously, i.e. (i) good crystallographic matching with the matrix; (ii) sufficient melt undercooling for grain initiation. For the former, the crystallographic orientation relationships (ORs) between TiCN and α-Mg can be predicted and evaluated by E2EM [43,44], where the interatomic spacing misfit between a pair of closed-packed rows $f_r$ and the interplanar spacing mismatch between a pair of closed-packed planes that

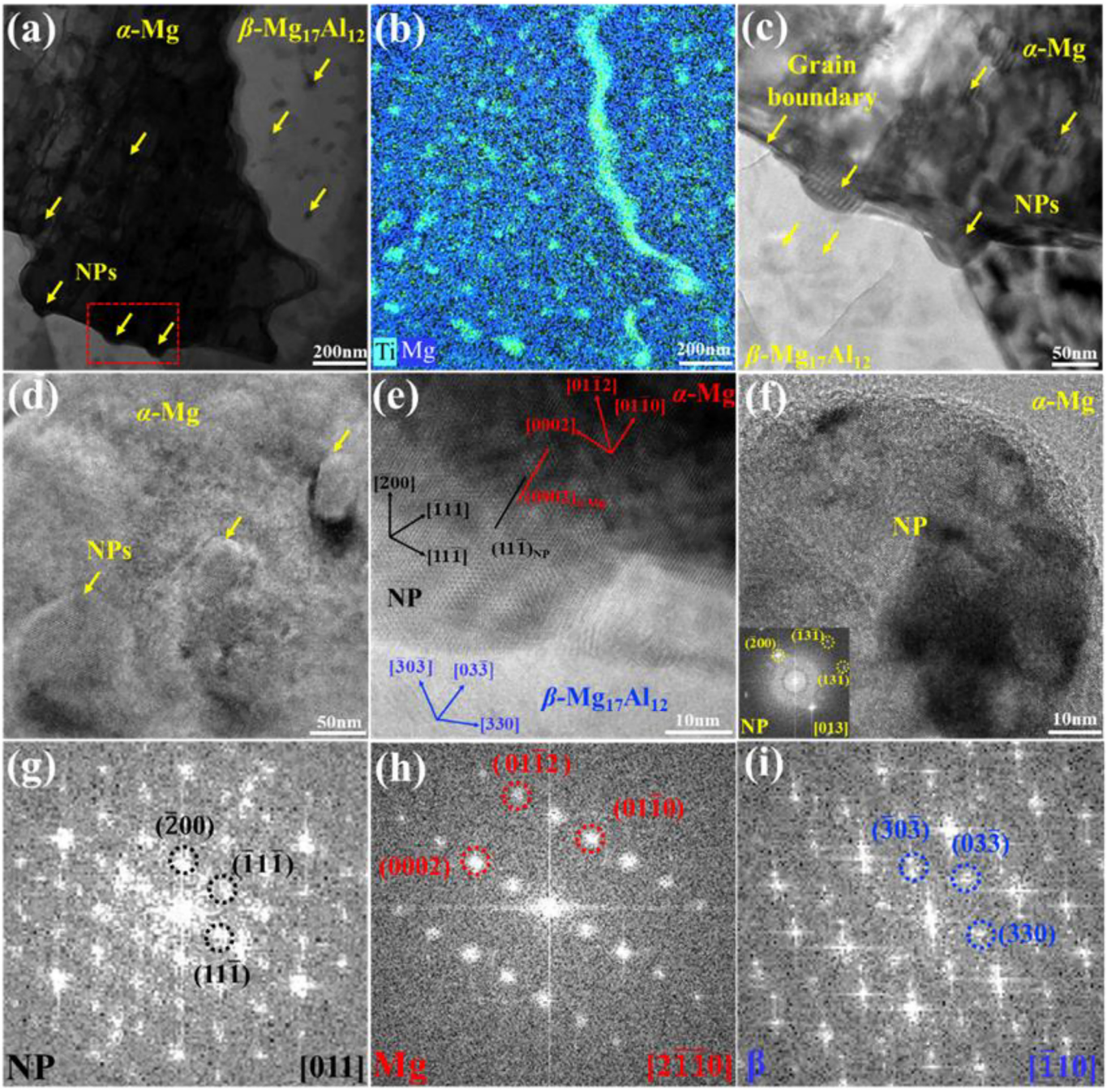


**Fig. 8.** (a) TEM bright-field image of NPs that are distributed in the AZ91 alloy with 2 vol% NP addition; (b) STEM mapping; (c) Magnified from (a); (d) HRTEM analysis of NPs within the interior of α-Mg grain; (e) HRTEM analysis of two interfaces between α-Mg and NP and between β-$Mg_{17}Al_{12}$ and NP; (f) HRTEM analysis of a NP located at grain boundary; (g), (h) and (i) are the fast Fourier transformation (FFT) of NP, α-Mg, and β-$Mg_{17}Al_{12}$ in (e), respectively;

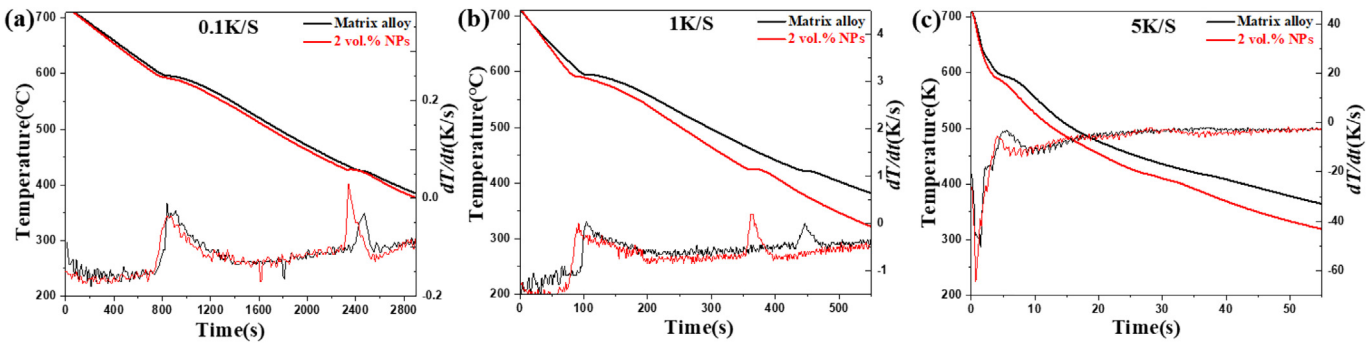


**Fig. 9.** The cooling curves of 2 vol% NPs alloy at different cooling rate: (a) 0.1 K/s; (b) 1 K/s; (c) 5 K/s. The time integration ($dT/dt$) of each curve is calculated and plotted in the bottom of each figure.

**Table 2**
The three characteristic temperatures extracted from cooling curves.

| Cooling rate (K/s) | Alloy | $T_{N,\alpha\text{-}Mg}$ (°C) | $T_{M,\alpha\text{-}Mg}$ (°C) | $\Delta T_{N,\alpha\text{-}Mg}$ (°C) | $T_{N,eu}$ (°C) | $T_{M,eu}$ (°C) | $\Delta T_{N,eu}$ (°C) |
|---|---|---|---|---|---|---|---|
| 0.1 | Base alloy | 597.8 | 597.2 | 0.6 | 427.6 | 427.2 | 0.4 |
| | 2.0 vol% NPs | 598 | 595 | 2.4 | 428.3 | 426.9 | 1.4 |
| 1 | Base alloy | 598.4 | 596.3 | 2.1 | 428.4 | 425.1 | 3.3 |
| | 2.0 vol% NPs | 599 | 591.6 | 6.4 | 430.2 | 424.2 | 6 |
| 5 | Base alloy | 599.8 | 595.5 | 4.3 | 430.6 | 419.3 | 11.3 |
| | 2.0 vol%NPs | 600.3 | 590.5 | 9.8 | 431.3 | 418 | 13.3 |

contain the rows $f_d$ should both satisfy the criteria of $f_r < 10\%$ and $f_d < 10\%$. The calculations show that there exist two possible ORs between α-Mg and TiCN as listed in Table 3, i.e. $[1120]_{Mg}//[110]_{TiCN}$, $(10\bar{1}1)_{Mg}//(111)_{TiCN}$ and $[1120]_{Mg}//[110]_{TiCN}$, $(0002)_{Mg}//(111)_{TiCN}$. More importantly, the HRTEM analysis of the nanoparticle within the interior of α-Mg in Fig. 12(a) and (b) may lead credence to the E2EM prediction as the observed OR of $[2110]_{Mg}//[011]_{NP}$, $(0002)_{Mg}//(111)_{NP}$ is consistent with the predicted one. Hence, the added TiCN particles may act as the nucleating particles to promote the heterogeneous nucleation of α-Mg from the crystallographic aspect. For the latter, based on the free-growth model [11], the undercooling for free growth $\Delta T_{fg}$ is inversely proportional to the particle diameter $d$, which is given by $\Delta T_{fg} = \frac{4\sigma}{\Delta S_v d}$ where $\sigma$ is the solid–liquid interfacial energy and $\Delta S_v$ is the entropy of fusion per unit volume. By calculation, the critical undercooling $\Delta T_{fg}$ for a TiCN nanoparticle with an average diameter of 50 nm is about 15.04 °C. From Table 2, however, it can be seen that the measured maximum undercoolings are less than 10 °C far below the required critical undercooling even for the samples solidified at the highest cooling rate of 5 K/s. Therefore, the added TiCN nanoparticles may not be activated to be effective nucleation sites in spite of high nucleation potency. Nevertheless, there remains a controversial issue of whether NP-clusters can be activated for heterogeneous nucleation if the critical undercooling can be reached due to their large size. Assuming that they can be activated, the crystallographic orientations of all

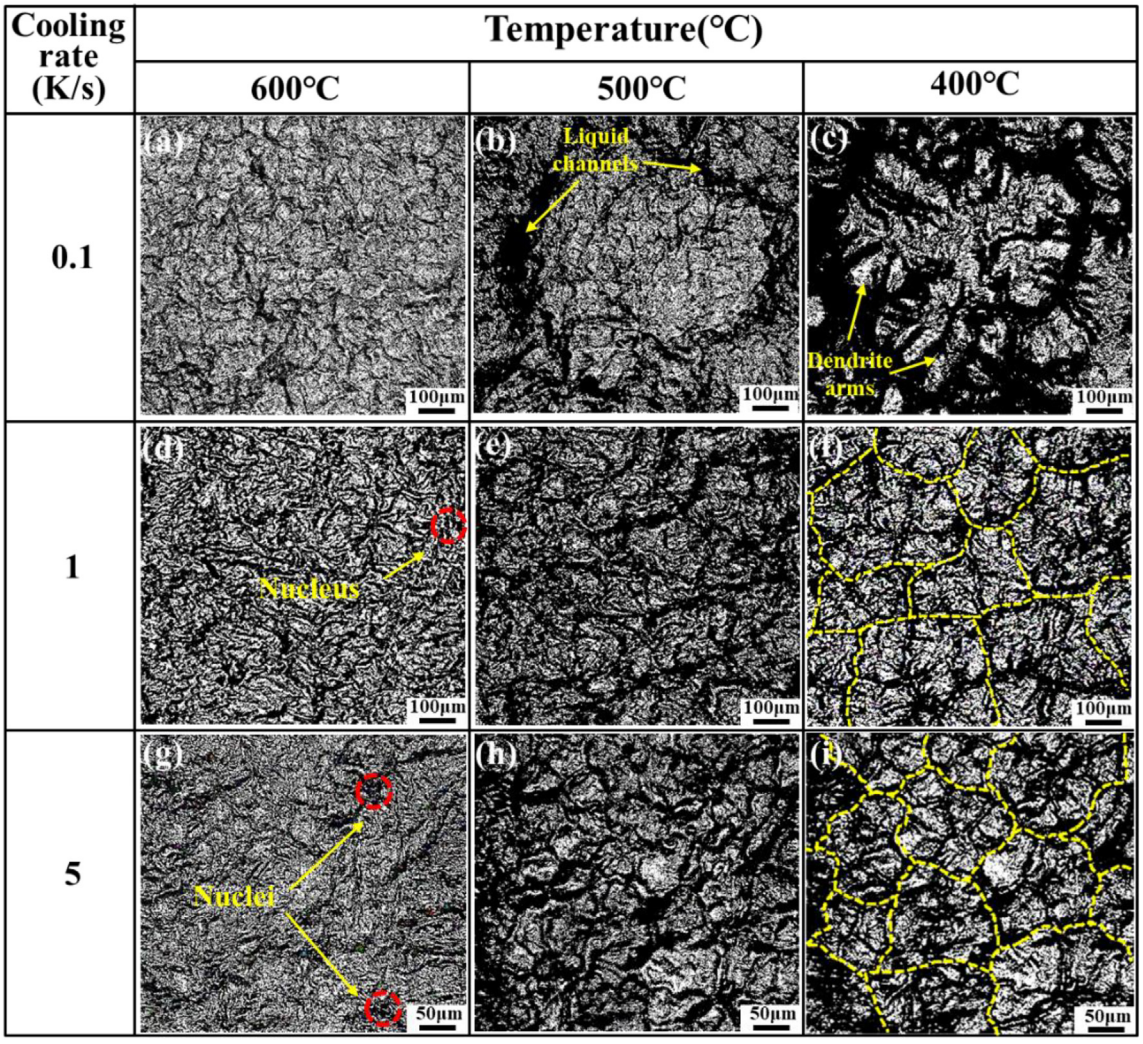


**Fig. 10.** In-situ observations of α-Mg grain growth in the matrix alloy produced at different cooling rates.

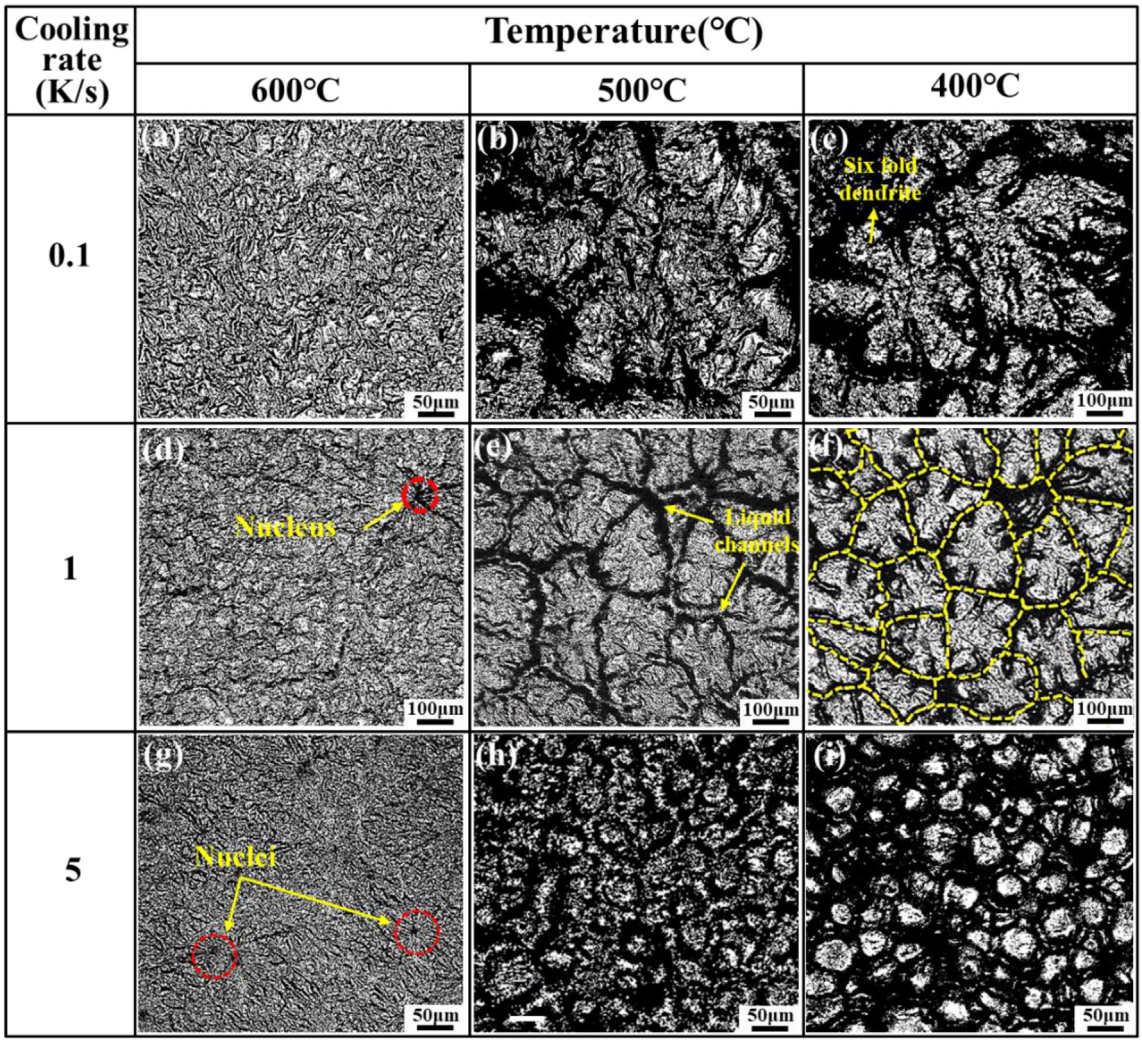


**Fig. 11.** In-situ observations of α-Mg grain growth in the 2.0 vol% NP-containing sample produced at different cooling rates.

nanoparticles within a NP-cluster must be consistent and their matching planes are expected to be parallelly exposed to α-Mg grains. Unfortunately, as depicted in Fig. 12(c) and (d), the selected area electron diffraction (SAED) of a NP-cluster exhibits only diffusive polycrystalline ring patterns, substantiating the polycrystalline nature of a NP-cluster with random orientation. As a result, the NP-cluster may not participate in the nucleation event as effective nucleating particles.

In fact, the enrichment of NPs at the interface can lead to a reduction in interfacial energy, which provides a driving force for the self-assembly of NPs onto the growing interfaces [21]. The interfacial energy is minimized when the interface is saturated by forming a NP-monolayer at the interface [45]. Based on the Boltzmann constant, temperature, nanoparticle size as well as their number density, they are capable of assembling rapidly onto the interfaces via Brownian motion. The smaller NP size, the higher Brownian velocity. In previous studies [19,21], the time factor $t_{np}$ was used as an indicator of the time for NP coverage onto the growing phases, and it is determined to be of the order of several milliseconds for the AZ91 alloy with 2.0 vol% NP addition. The rapid formation of NP-monolayer can greatly restrict grain growth at the initial stage of solidification. As solidification proceeds,

**Table 3**
The possible orientations between Mg and TiCN predicted by E2EM.

| Crystal structure and lattice parameters | Matching planes | $f_p$ (%) | Matching directions | $f_p$ (%) | *OR* |
|---|---|---|---|---|---|
| TiCN FCC | $(10\bar{1}1)_{Mg}/(111)_{TiCN}$ | −0.4 | | | |
| a = 0.4264 nm | $(0002)_{Mg}/(111)_{TiCN}$ | 5.4 | | | |
| | $(10\bar{1}1)_{Mg}/(200)_{TiCN}$ | 13 | | | $[11\bar{2}0]_{Mg}/[110]_{TiCN}$ |
| | $(10\bar{1}1)_{Mg}/(220)_{TiCN}$ | 23.2 | $[1120]_{Mg}/[110]_{TiCN}$ | 6.4 | $(10\bar{1}1)_{Mg}/(111)_{TiCN}$ |
| Mg HCP | $(10\bar{1}0)_{Mg}/(111)_{TiCN}$ | 11.3 | $[1120]_{Mg}/[100]_{TiCN}$ | 50.6 | |
| a = 0.3209 nm | $(10\bar{1}0)_{Mg}/(200)_{TiCN}$ | 23.24 | $1120]_{Mg}/[112]_{TiCN}$ | 62.8 | $[11\bar{2}0]_{Mg}/[110]_{TiCN}$ |
| c = 0.5211 nm | $(10\bar{1}0)_{Mg}/(220)_{TiCN}$ | 45.72 | | | $(0002)_{Mg}/(111)_{TiCN}$ |
| | $(0002)_{Mg}/(200)_{TiCN}$ | 18.1 | | | |
| | $(0002)_{Mg}/(220)_{TiCN}$ | 11.3 | | | |

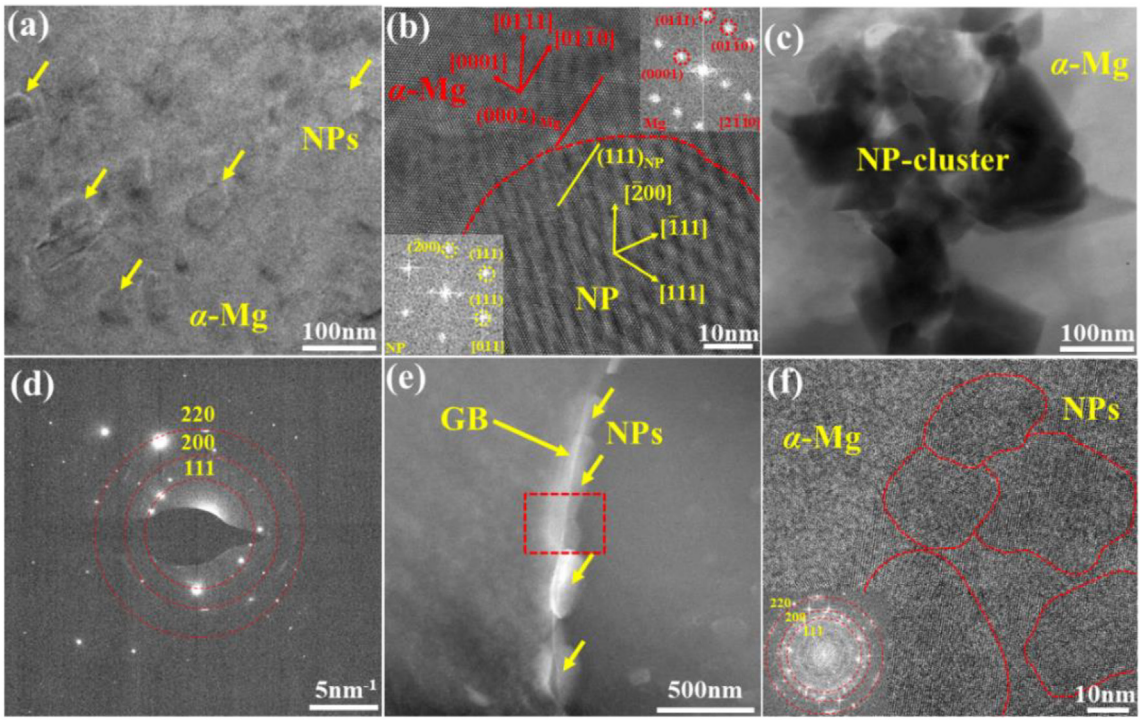


**Fig. 12.** (a) TEM bright-field image of NPs within the interior of α-Mg; (b) HRTEM image showing the coherent interface between NP and α-Mg; (c) TEM bright-field images of NP-cluster inside α-Mg grain; (d) Selected area electron diffraction (SAED) of NP-cluster in (c); (e) TEM bright-field image exhibiting a NP-layer covering the grain boundary; (f) HRTEM image of the grain boundary in (e). The inset in (f) displays the polycrystalline nature of a NP-cluster with random orientation.

more nanoparticles would be pushed ahead of the solid/liquid interface, which could lead to the transition of NP-layer from monolayer to multilayer. Assuming α-Mg grain grows to the point where the grain boundary is entirely covered by a NP-monolayer, its grain size can be determined by $\Delta = \frac{2nd}{\sqrt{3}V_f}$ [46],where Δ is the grain size, $d$ is the diameter of nanoparticle and $V_f$ is volume fraction of NPs. Given $V_f = 0.02$ and $d =$ 50 nm, the Δ is calculated to be 9.1 μm in the present work. Taking into account the measured size of 36 μm, the α-Mg grain with the size of 36 μm would be covered by roughly four layers of NPs. Fig. 12(e) exhibits the bright-field TEM image of a typical NP-layer at the grain boundary. It has a width of approximately 200 nm, which is exactly four times as large as the average diameter of NPs. According to the crystallographic information provided in Fig. 12(f), the multilayer structure of NP-layer can be confirmed, which is in good agreement with the theoretical analysis. Conclusively, the NPs assembling onto the surface of growing grains of α-Mg can effectively retard the transport of solutal atoms and greatly restrict their growth, thus leading to a significant grain refinement of AZ91 alloys.

On the other hand, the predictions using E2EM, as listed in Table 4, show that TiCN has a poor nucleation potency for β-$Mg_{17}Al_{12}$. And the HRTEM analysis in Fig. 8(e) also demonstrates that there is no crystallographic matching between NP and β-$Mg_{17}Al_{12}$. Thus, TiCN nanoparticles may not act as nucleating particles for the heterogeneous nucleation of β phases. Instead, the presence of nanoparticles along grain boundaries can hamper the growth of eutectic phases, thus resulting in the refinement of β phases.

### 4.2. Modelling of NP-induced grain refinement

The microstructural observation demonstrates that a large proportion of nanoparticles are distributed along the grain boundaries, based on which the growth mechanism of α-Mg grains can be elucidated in terms of the NP effects on the solute diffusion. Fig. 13(a) is a schematic illustration of two growing equiaxed α-Mg dendrites in an undercooled melt, and each dendrite can be divided into three regions including solid dendrite (Region 1), interdendritic liquid within a grain envelope marked by radius $R_g$ (Region 2) and free liquid with a solute diffusion zone outside the grain envelope (Region 3) [47].

When the α-Mg grains begin to nucleate, the neighboring nanoparticles dispersed in the melt, driven by the reduction in interfacial energy,

**Table 4**
The possible orientations between β-$Mg_{17}Al_{12}$ and TiCN predicted by E2EM.

| Crystal structure and lattice parameters | Matching planes | $f_p$ (%) | Matching directions | $f_d$ (%) | *OR* |
|---|---|---|---|---|---|
| TiCN FCC | $(330)_\beta/(111)_{TiCN}$ | 0.7 | $[001]_\beta/[100]_{TiCN}$ | 79.8 | – |
| a = 0.4264 nm | $(330)_\beta/(200)_{TiCN}$ | 14.01 | $[001]_\beta/[110]_{TiCN}$ | 71.4 | |
| | $(330)_\beta/(220)_{TiCN}$ | 39.2 | $[001]_\beta/[112]_{TiCN}$ | 50.5 | |
| | $(332)_\beta/(111)_{TiCN}$ | −9.9 | $[110]_\beta/[100]_{TiCN}$ | 85.7 | |
| β-$Mg_{17}Al_{12}$ FCC | $(332)_\beta/(200)_{TiCN}$ | 4.8 | $[110]_\beta/[110]_{TiCN}$ | 79.8 | |
| a = 1.0561 nm | $(332)_\beta/(220)_{TiCN}$ | 32.68–72.18 | $[110]_\beta/[112]_{TiCN}$ | 65.1 | |
| | $(721)_\beta/(111)_{TiCN}$ | | $[111]_\beta/[100]_{TiCN}$ | 76.6 | |
| | $(721)_\beta/(200)_{TiCN}$ | −49.44 | $[111]_\beta/[110]_{TiCN}$ | 70.8 | |
| | $(721)_\beta/(220)_{TiCN}$ | −5.4 | $[111]_\beta/[112]_{TiCN}$ | 42.8 | |

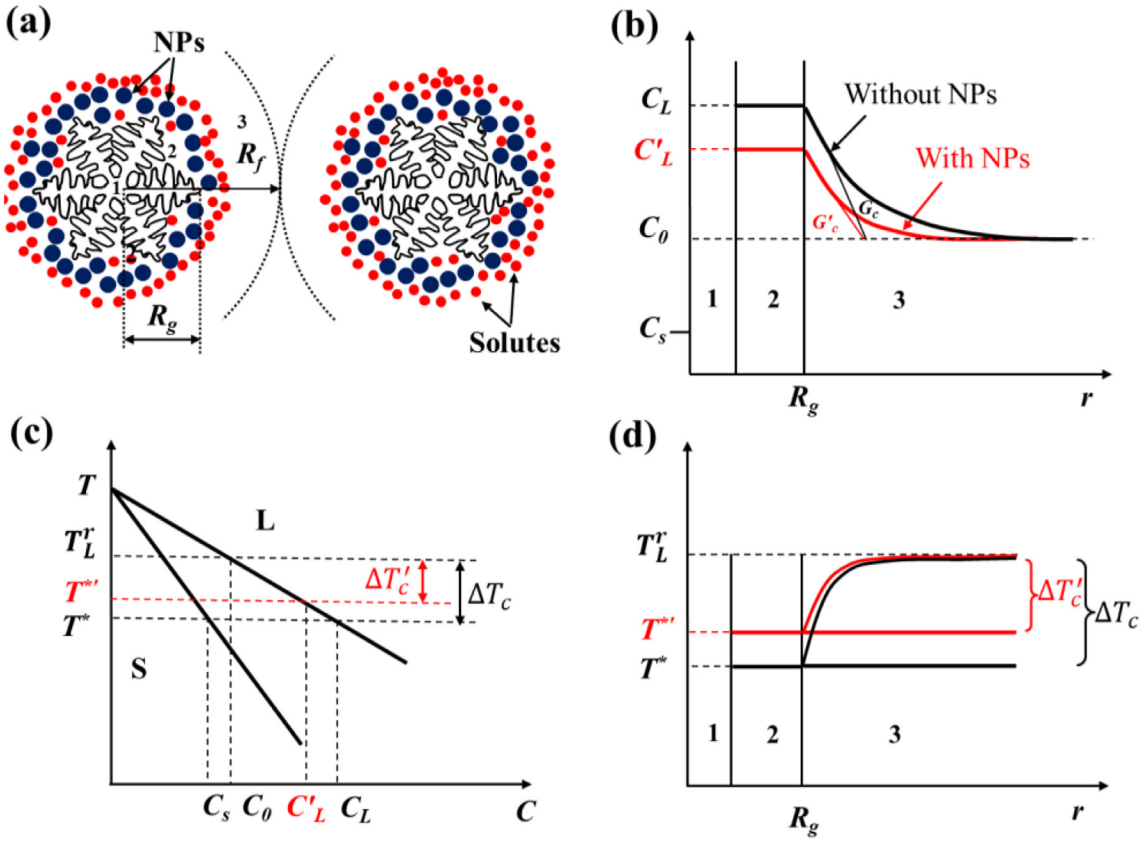


**Fig. 13.** (a) The schematic of α-Mg dendrite growth process with marked three regions 1, 2, 3, indicating a solid dendrite, an interdendritic liquid within the grain envelope marked by radius $R_g$, and the free liquid with a solute diffusion zone outside the grain envelope, respectively. $R_g$ refers to the radius of growing grains at any growing time $t$ and $R_f$ is the final grain radius after the occurrence of impingement; (b) Solute profiles with partition coefficient k < 1 for the AZ91 alloys with and without NP addition; (c) Binary phase diagram with partition coefficient k < 1; (d) Temperature fields ahead of a dendrite front.

can rapidly self-assemble onto the surface of α-Mg grain until a NP-monolayer is established. The formed NP layer can act as a diffusion barrier to prevent solute atoms from transporting onto the growing interface, leading to the reduction in solute concentration at the dendrite tip. In the case of the partition coefficient k < 1, the solute concentration at the dendrite tip is thus decreased from $C_L$ to $C_L$', connected with the solute concentration gradient in reigon 3 decreasing from $G_C$ to $G'_C$ as shown in Fig. 13(b).

Fig. 13(c) exhibits the binary phase diagram with partition coefficient k < 1, in which the constitutional undercooling $\Delta T_c$ is given by $\Delta T_c = T_L^r - T^*$, where $T_L^r$ is the liquidus temperature at a curved interface and $T^*$ is the interface temperature at the dendrite tip [48]. Given that thermal undercooling and curvature undercooling are insignificant in an isothermal melt, solutal undercooling is only considered as the effect on the grain growth. The variation of solute concentration at the interface due to the presence of NPs results in the increase of interface temperature from $T^*$ to $T^{*\prime}$, accompanied by the decrease of constitutional undercooling from $\Delta T_c$ to $\Delta T_c'$ as depicted in Fig. 13(d). The decreased constitutional undercooling has a strong effect in reducing the growth rate of α-Mg dendrites and thus limiting the grain size.

Another important factor affecting grain growth is grain impingement. At the initial stage of solidification, the grains are isolated from each other and can grow unimpeded by surrounding grains. As solidification proceeds, the growing grains begin to impinge on one another. As soon as the hard impingement occurs, the grain growth is terminated and final grain size is achieved. For a better understanding, the grain impingement is shown schematically in Fig. 13(a). $R_g$ is the instant grain radius at any growth time $t$, and $R_f$ is the final grain radius after grain impingement. As the occurrence of impingement signifies the end of grain growth, the time when impingement occurs can be taken as the time for grain growth, which is termed impingement time in this work.

The NP-induced solute concentration variation and the impingement of dendrites are two critical factors determining the growth of α-Mg grains. Taking them into consideration, an analytical model is proposed to quantitatively account for the growth behavior of α-Mg grains and established as $R = \frac{\xi_p k D V_c^2 t^{*3}}{3\Gamma m C_0 (k-1)\pi^2}$. The parameters used for model calculation are listed in Supplementary Table S1 and more details about the growth model are provided in Supplementary note 1. It can be seen that the grain size is proportional to the solute-diffusion factor $\xi_p$, the cooling rate $V_c$ and the impingement time $t^*$.

The present model theoretically accounts for the combined effect of NPs and grain impingement on the grain size due to growth restriction by NP assembly ( $\xi_p$) onto the interface and the impingement ($t^*$) with surrounding grains. Apart from $\xi_p$ and $t^*$, other important parameters influencing grain size include the cooling rate $V_c$, and the growth restriction parameter $Q$ ($Q = mC_0(k-1)$) [10], which can be determined from the cooling curve and the phase diagram, respectively. It can be seen from the model that for given alloy composition and solidification conditions, the grain refinement effect largely depends on the solute-diffusion factor $\xi_p$. In the model, $\xi_p$ is merely dependent on the addition level of nanoparticles. Once the addition level is given, the $\xi_p$ is invariable. It can be determined using the model from the measured grain sizes produced at different cooling rates. Fig. 14(a) exhibits the variation of $\xi_p$with NP contents. It can be seen that $\xi_p$ is decreased to the minimum when the addition level is raised up to 2.0 vol%. Fig. 14(b) shows

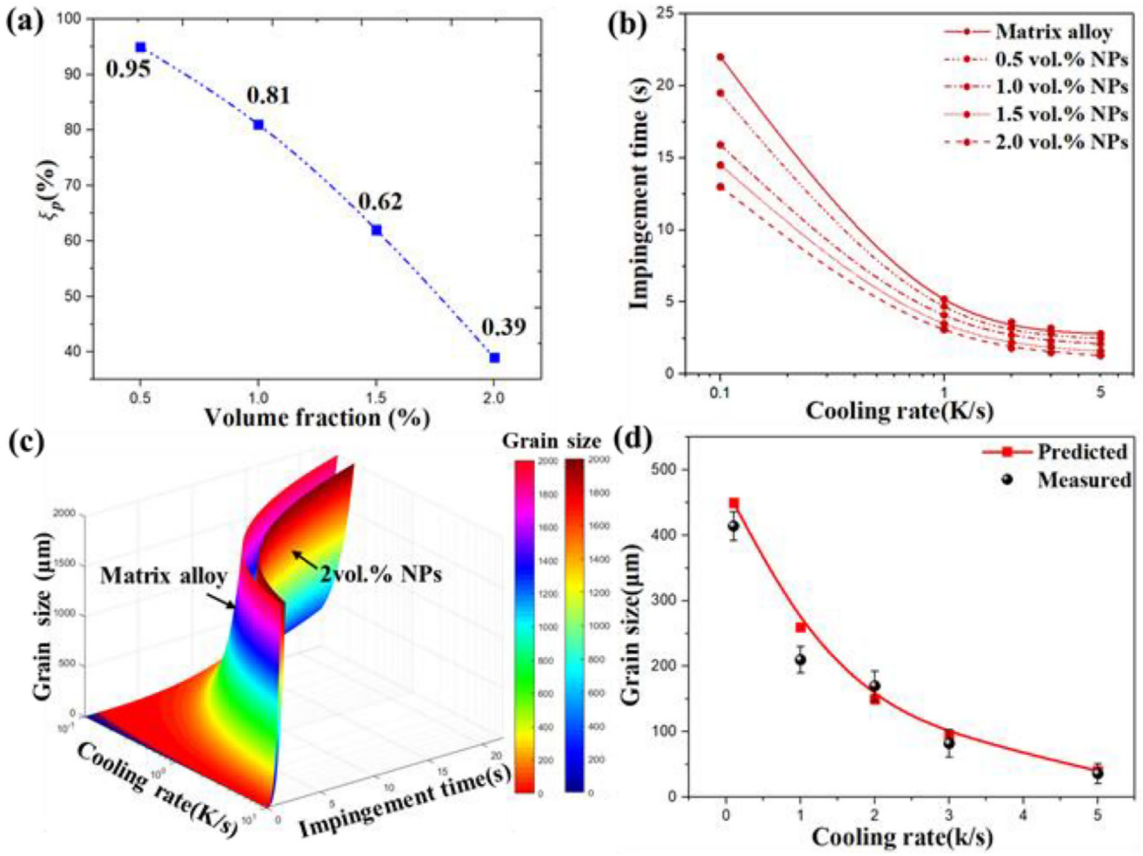


**Fig. 14.** (a) Dependences of $\xi_p$ on NP addition levels; (b) Impingement time as functions of cooling rate and NP addition level; (c) Correlations among the grain size, cooling rate and impingement time in a three-dimensional coordinates for matrix alloy and 2 vol% NP-containing sample, respectively; (d) Comparison of the measured grain sizes of 2 vol% NP-containing sample with the predictions.

the measured impingement time as a function of cooling rate and NP addition level. The results show that for a given NP addition level, the higher the cooling rate is, the less the impingement time. Also obvious is that the impingement time for NP-containing sample produced at the same cooling rate is decreased with increasing NP addition levels. For clarity, the correlations among grain size, cooling rate and impingement time in three-dimensional coordinates are illustrated in Fig. 14(c). It is clear that the "curved surface" for 2.0 vol% NP-containing sample is located below that for matrix alloy, implying that small grain size can be obtained upon addition of 2.0 vol% NPs on the condition of the same cooling rate and impingement time. Nevertheless, the actual impingement time for 2.0 vol% NP-containing sample is much lower than that for matrix alloy even at the same cooling rate as shown in Fig. 14(b). Thus, the NP addition may lead to finer grain size. Fig. 14(d) shows the comparison between the measured grain size and the prediction. The prediction is in good agreement with the experimental results, confirming the validity of the model.

The model analysis shows that the presence of nanoparticles could not only cause the reduction in solute concentration gradient at dendrite tips, but also affect the impingement between grains. On the one hand, the smaller $\xi_p$ is, the lower the solute concentration gradient and the growth velocity of α-Mg. The reduced growth rate could stifle the release of latent heat from growing α-Mg grains. Therefore, recalescence would occur at a low temperature, which in turn provides a large undercooling for the continuous nucleation of grains and thus leads to an increase in grain number density. It is noted that the experimental results listed in Table 2 demonstrate that the measured undercooling before recalescence is indeed increased after NP addition. On the other hand, the higher grain density could lead to the smaller grain interval, which accelerates the grain impingement and reduces the impingement time. It can be safely speculated that an increase in cooling rate or NP addition level may induce grain refinement and lead to an increase in grain number density and thus a decrease in impingement time, which may explicate the variation trends of impingement time with cooling rate and addition level. Overall, the NIGC is a competition between grain growth and grain impingement. With increasing NP addition levels, the growth velocity of grains is decreased and the undercooling before recalescence is increased, which multiplies the nucleation events and accelerates the grain impingement, so that fine grains can be achieved in the solidified microstructure.

## 5. Conclusion

In this study, the NP-induced grain refinement phenomenon of AZ91 alloys are investigated systemically. Combined with the experimental results and theoretical model analysis, the main conclusions could be summarized as follows:

(1) The added nanoparticles are distributed in matrix in three ways, i.e. along the grain boundaries, inside the α-Mg grains and within the interior of β phases.
(2) From the perspective of heterogeneous nucleation, the nanoparticles with an average size of 50 nm can not act as the effective nucleation sites. Instead, the growth control induced by multilayer of NPs covering the surface of α-Mg could be the main refining mechanism for AZ91 alloys.
(3) The growth kinetics of α-Mg, based on two crucial factors, i.e. solute concentration gradient at dendrite tip and grain impingement, is established and given by $= \frac{\xi_p k D V_c^2 t^{*3}}{3\Gamma m C_0 (k-1)\pi^2}$.

(4) The more NPs added to the melt, the lower the solute concentration gradient at dendrite tip and the growing velocity of grains. The reduced growth rate could increase the nucleation events and promote the grain impingement, leading to significant grain refinement of AZ91 alloys.

## Declaration of competing interest

We declare that we do not have any commercial or associative interest that represents a conflict of interest in connection with the work submitted.

## Acknowledgements

The present study was sponsored by the National Natural Science Foundation of China, People's Republic of China (NSFC) under Grant no. 51804197, Grant no. 51674166 and U1902220. Startup Fund for Youngman Research at SJTU (SFYR at SJTU).

## Data availability statement

All data included in this study are available upon request by contact with the corresponding author.

## Author's contribution statement

As being the authors of this research paper, we declare that the work is entirely original, any raw data exiting in the article can be provided. Besides, the work has never been submitted/published in any other journal.

## Appendix A. Supplementary data

Supplementary data to this article can be found online at https://doi.org/10.1016/j.matdes.2020.109146.

## References

[1] Y. Kojima, T. Aizawa, S. Kamado, K. Higashi, Progressive steps in the platform science and technology for advanced magnesium alloys, Mater. Sci. Forum, Trans Tech Publ 2003, pp. 3–20.
[2] T.M. Pollock, Weight loss with magnesium alloys, Science 328 (5981) (2010) 986–987.
[3] H. Friedrich, S. Schumann, Research for a “new age of magnesium” in the automotive industry, J. Mater. Process. Technol. 117 (3) (2001) 276–281.
[4] Y. Ali, D. Qiu, B. Jiang, F. Pan, M.-X. Zhang, Current research progress in grain refinement of cast magnesium alloys: a review article, J. Alloys Compd. 619 (2015) 639–651.
[5] R. Günther, C. Hartig, R. Bormann, Grain refinement of AZ31 by (SiC) P: theoretical calculation and experiment, Acta Mater. 54 (20) (2006) 5591–5597.
[6] L. Lu, A. Dahle, D. StJohn, Grain refinement efficiency and mechanism of aluminium carbide in Mg–Al alloys, Scr. Mater. 53 (5) (2005) 517–522.
[7] H. Fu, M.-X. Zhang, D. Qiu, P. Kelly, J. Taylor, Grain refinement by AlN particles in Mg–Al based alloys, J. Alloys Compd. 478 (1–2) (2009) 809–812.
[8] B. Jiang, W. Liu, D. Qiu, M.-X. Zhang, F. Pan, Grain refinement of Ca addition in a twin-roll-cast Mg–3Al–1Zn alloy, Mater. Chem. Phys. 133 (2–3) (2012) 611–616.
[9] D. Qiu, M.-X. Zhang, J. Taylor, P. Kelly, A new approach to designing a grain refiner for Mg casting alloys and its use in Mg–Y-based alloys, Acta Mater. 57 (10) (2009) 3052–3059.
[10] D.H. StJohn, M. Qian, M.A. Easton, P. Cao, Z. Hildebrand, Grain refinement of magnesium alloys, Metall. Mater. Trans. A 36 (7) (2005) 1669–1679.
[11] A. Greer, A. Bunn, A. Tronche, P. Evans, D. Bristow, Modelling of inoculation of metallic melts: application to grain refinement of aluminium by Al–Ti–B, Acta Mater. 48 (11) (2000) 2823–2835.
[12] H. Dieringa, Properties of magnesium alloys reinforced with nanoparticles and carbon nanotubes: a review, J. Mater. Sci. 46 (2) (2011) 289–306.
[13] W. Sillekens, D. Jarvis, A. Vorozhtsov, V. Bojarevics, C. Badini, M. Pavese, S. Terzi, L. Salvo, L. Katsarou, H. Dieringa, The ExoMet project: EU/ESA research on high-performance light-metal alloys and nanocomposites, Metall. Mater. Trans. A 45 (8) (2014) 3349–3361.
[14] D. Wang, M.P. De Cicco, X. Li, Using diluted master nanocomposites to achieve grain refinement and mechanical property enhancement in as-cast Al–9Mg, Mater. Sci. Eng. A 532 (2012) 396–400.
[15] L.-Y. Chen, J.-Y. Peng, J.-Q. Xu, H. Choi, X.-C. Li, Achieving uniform distribution and dispersion of a high percentage of nanoparticles in metal matrix nanocomposites by solidification processing, Scr. Mater. 69 (8) (2013) 634–637.
[16] K. Wang, H. Jiang, Y. Wang, Q. Wang, B. Ye, W. Ding, Microstructure and mechanical properties of hypoeutectic Al–Si composite reinforced with TiCN nanoparticles, Mater. Des. 95 (2016) 545–554.
[17] B. Kowalczyk, K.J. Bishop, I. Lagzi, D. Wang, Y. Wei, S. Han, B.A. Grzybowski, Charged nanoparticles as supramolecular surfactants for controlling the growth and stability of microcrystals, Nat. Mater. 11 (3) (2012) 227–232.
[18] L.-Y. Chen, J.-Q. Xu, X.-C. Li, Controlling phase growth during solidification by nanoparticles, Mater. Res. Lett. 3 (1) (2015) 43–49.
[19] K. Wang, H.Y. Jiang, Y.W. Jia, H. Zhou, Q.D. Wang, B. Ye, W.J. Ding, Nanoparticle-inhibited growth of primary aluminum in Al–10Si alloys, Acta Mater. 103 (2016) 252–263.
[20] E. Guo, S. Shuai, D. Kazantsev, S. Karagadde, A. Phillion, T. Jing, W. Li, P.D. Lee, The influence of nanoparticles on dendritic grain growth in Mg alloys, Acta Mater. 152 (2018) 127–137.
[21] L.-Y. Chen, J.-Q. Xu, H. Choi, H. Konishi, S. Jin, X.-C. Li, Rapid control of phase growth by nanoparticles, Nat. Commun. 5 (1) (2014) 1–9.
[22] G. Chai, L. BÄckerud, T. RØlland, L. Arnberg, Dendrite coherency during equiaxed solidification in binary aluminum alloys, Metall. Mater. Trans. A 26 (4) (1995) 965–970.
[23] S. Offerman, N. Van Dijk, J. Sietsma, S. Grigull, E. Lauridsen, L. Margulies, H. Poulsen, M.T. Rekveldt, S. Van der Zwaag, Grain nucleation and growth during phase transformations, Science 298 (5595) (2002) 1003–1005.
[24] G. Wang, M. Dargusch, M. Qian, D. Eskin, D.H. StJohn, The role of ultrasonic treatment in refining the as-cast grain structure during the solidification of an Al–2Cu alloy, J. Cryst. Growth 408 (2014) 119–124.
[25] G. Levi, M. Bamberger, W. Kaplan, Wetting of porous titanium carbonitride by Al–Mg–Si alloys, Acta Mater. 47 (14) (1999) 3927–3934.
[26] S. Shabestari, M. Malekan, Assessment of the effect of grain refinement on the solidification characteristics of 319 aluminum alloy using thermal analysis, J. Alloys Compd. 492 (1–2) (2010) 134–142.
[27] Y. Zhang, H. Zheng, Y. Liu, L. Shi, R. Xu, X. Tian, Cluster-assisted nucleation of silicon phase in hypoeutectic Al–Si alloy with further inoculation, Acta Mater. 70 (2014) 162–173.
[28] E. Guo, L. Wang, Y. Feng, L. Wang, Y. Chen, Effect of cooling rate on the microstructure and solidification parameters of Mg–3Al–3Nd alloy, J. Therm. Anal. Calorim. 135 (4) (2019) 2001–2008.
[29] Y.C. Guo, K.B. Nie, X.K. Kang, K.K. Deng, J.G. Han, Z.H. Zhu, Achieving high-strength magnesium matrix nanocomposite through synergistical effect of external hybrid (SiC+TiC) nanoparticles and dynamic precipitated phase, J. Alloys Compd. 771 (2019) 847–856.
[30] Y.M. Kim, L. Wang, B.S. You, Grain refinement of Mg–Al cast alloy by the addition of manganese carbonate, J. Alloys Compd. 490 (1–2) (2010) 695–699.
[31] S.F. Liu, L.Y. Liu, L.G. Kang, Refinement role of electromagnetic stirring and strontium in AZ91 magnesium alloy, J. Alloys Compd. 450 (1–2) (2008) 546–550.
[32] K.B. Nie, X.J. Wang, K. Wu, X.S. Hu, M.Y. Zheng, Development of SiCp/AZ91 magnesium matrix nanocomposites using ultrasonic vibration, Mater. Sci. Eng. A 540 (2012) 123–129.
[33] C. Zhang, Z. Li, Y. Ye, Y. Yuan, D. Fang, H. Wu, W. Li, Interaction of nanoparticles and dislocations with Mg17Al12 precipitates in n-SiCp/AZ91D magnesium matrix nanocomposites, J. Alloys Compd. 815 (2020).
[34] X. Wang, N. Wang, L. Wang, X. Hu, K. Wu, Y. Wang, Y. Huang, Processing, microstructure and mechanical properties of micro-SiC particles reinforced magnesium matrix composites fabricated by stir casting assisted by ultrasonic treatment processing, Mater. Des. 57 (2014) 638–645.
[35] P. Xiao, Y. Gao, F. Xu, S. Yang, B. Li, Y. Li, Z. Huang, Q. Zheng, An investigation on grain refinement mechanism of TiB2 particulate reinforced AZ91 composites and its effect on mechanical properties, J. Alloys Compd. 780 (2019) 237–244.
[36] L. Wang, Y.M. Kim, J. Lee, B.S. You, Improvement in rollability of AZ91 magnesium alloy by carbon addition, Mater. Sci. Eng. A 528 (3) (2011) 943–949.
[37] O. Sedighi, S. Shabestari, F. Yavari, Investigation on the effect of Sn on solidification and microstructure of AZ91 magnesium alloy using cooling curve thermal analysis, Thermochim. Acta 667 (2018) 165–172.
[38] J. Wang, X. Li, Simultaneously improving strength and ductility of AZ91-type alloys with minor Gd addition, J. Alloys Compd. 803 (2019) 689–699.
[39] A. Boby, A. Srinivasan, U.T.S. Pillai, B.C. Pai, Effect of Sb, Sn and Pb additions on the microstructure and mechanical properties of AZ91 alloy, Mater. Sci. Forum, Trans Tech Publ 2015, pp. 375–378.
[40] B. Sahoo, S. Panigrahi, Effect of in-situ (TiC-TiB2) reinforcement on aging and mechanical behavior of AZ91 magnesium matrix composite, Mater. Charact. 139 (2018) 221–232.
[41] Y. Liu, X. Liu, B. Xiufang, Grain refinement of Mg–Al alloys with Al4C3–SiC/Al master alloy, Mater. Lett. 58 (7–8) (2004) 1282–1287.
[42] P. Song, G.-h. Wu, W.-c. Liu, L. Zhang, Y. Zhang, H. Conrad, W.-j. Ding, Influence of cooling rate on solidification behavior of sand-cast Mg–10Gd–3Y–0.4 Zr alloy, Trans. Nonferrous Metals Soc. China 24 (11) (2014) 3413–3420.
[43] M.-X. Zhang, P. Kelly, M. Qian, J. Taylor, Crystallography of grain refinement in Mg–Al based alloys, Acta Mater. 53 (11) (2005) 3261–3270.

[44] M.-X. Zhang, P.M. Kelly, M.A. Easton, J.A. Taylor, Crystallographic study of grain refinement in aluminum alloys using the edge-to-edge matching model, Acta Mater. 53 (5) (2005) 1427–1438.
[45] M. Cui, T. Emrick, T.P. Russell, Stabilizing liquid drops in nonequilibrium shapes by the interfacial jamming of nanoparticles, Science 342 (6157) (2013) 460–463.
[46] A. Greer, Overview: application of heterogeneous nucleation in grain-refining of metals, J. Chem. Phys. 145 (21) (2016) 211704.
[47] M. Rappaz, P. Thevoz, Solute diffusion model for equiaxed dendritic growth, Acta Metall. 35 (7) (1987) 1487–1497.
[48] D. Shu, B. Sun, J. Mi, P. Grant, A quantitative study of solute diffusion field effects on heterogeneous nucleation and the grain size of alloys, Acta Mater. 59 (5) (2011) 2135–2144.